

HST-STIS Observations of the Cygnus Loop: Spatial Structure of a Non-radiative Shock¹

Ravi Sankrit², William P. Blair², John C. Raymond³, Knox S. Long⁴

ABSTRACT

We present a spatially-resolved ultraviolet spectrum of a non-radiative shock front in the Cygnus Loop, obtained with the Space Telescope Imaging Spectrograph (STIS) on board the Hubble Space Telescope (HST). The spectrum covers the wavelength range 1118 Å - 1716 Å with an effective spectral resolution of ~ 12 Å. The $0''.1$ spatial resolution of these data provides a huge improvement over earlier ultraviolet spectra, allowing us to study the spatial distribution of high ionization line emission directly behind the shock front. We are able to isolate individual shock features in our spectrum by comparing the STIS spectrum with a WFPC2- $H\alpha$ image of the region. Isolating the brightest shock tangency, we identify lines of N V $\lambda 1240$, C IV $\lambda 1549$, He II $\lambda 1640$, O V $\lambda 1371$, O IV] and Si IV $\lambda 1400$, and N IV] $\lambda 1486$, as well as the hydrogen 2-photon continuum. The N V emission peaks $\sim 0''.3$ behind the C IV and He II emission and is spatially broader. Also, the observed line ratios of C IV and He II to N V are higher in our bright shock spectrum than in previous observations of the same filament obtained through much larger apertures (and little or no spatial resolution), indicating that there must be a more widely distributed component of the N V emission. We calculate shock models and show that the observed separation between the C IV and N V emission zones and observed line intensities constrain the combinations of shock velocity and pre-shock density that are allowed.

¹Based on observations with the NASA/ESA *Hubble Space Telescope*, obtained at the Space Telescope Science Institute, which is operated by AURA, Inc., under NASA contract NAS5-26555.

²Department of Physics and Astronomy, The Johns Hopkins University, 3400 N. Charles St., Baltimore, MD 21218

³Harvard-Smithsonian Center for Astrophysics, 60 Garden St., Cambridge, MA 02138

⁴Space Telescope Science Institute, 3700 San Martin Drive, Baltimore, MD 21218

Subject headings: ISM: individual (Cygnus Loop) — ISM: nebulae — ISM: supernova remnants — Shock waves

1. Introduction

Faint filaments dominated by Balmer line emission are seen around much of the periphery of the Cygnus Loop supernova remnant (SNR). These filaments are due to shocks driven by the supernova blastwave into partly neutral material. The Balmer lines, of which $H\alpha$ is the strongest, are collisionally excited in a narrow zone behind the shock front (Chevalier, Kirshner & Raymond 1980). In the hot post-shock region, different elements are producing resonance line emission (mainly in the ultraviolet) as they move to higher stages of ionization. The shocked gas has not had time to recombine and cool radiatively and so these shocks are termed “non-radiative”. The Balmer lines and the ultraviolet line spectrum can be used as diagnostics to infer properties of the shock wave and conditions in the preshock gas (e.g. Raymond 1991).

One particular Balmer filament, the brightest in the northeast region of the Cygnus Loop, has been the subject of detailed study. Based on the width of the $H\alpha$ line, and on line strengths obtained from ground based optical spectra and ultraviolet spectra taken with the *International Ultraviolet Explorer* (IUE), Raymond et al. 1983; henceforth RBF_G inferred a preshock density of $\sim 2 \text{ cm}^{-3}$ and shock velocities of 210 km s^{-1} (for the case of rapid equilibration between ions and electrons), and 170 km s^{-1} (for the case of slower Coulomb equilibration between ions and electrons). Fesen & Itoh 1985 used the same IUE data and optical spectra of a different location along the same filament and favored a 190 km s^{-1} shock running into gas with a density of 1 cm^{-3} . The filament was later observed with the *Hopkins Ultraviolet Telescope* (HUT) and the far ultraviolet line strengths were found to be best fit by a 180 km s^{-1} shock, a preshock density of 2 cm^{-3} and rapid equilibration of electrons and ions behind the shock (Long et al. 1992; henceforth L92). However, in the same study, the ratio of line strengths in the O VI $\lambda\lambda 1032, 1038$ doublet indicated significant resonant scattering along the line of sight and implied a preshock density between 5 cm^{-3} and 12 cm^{-3} . Hester, Raymond & Blair 1994; henceforth HRB presented an extensive study of Balmer filaments in the NE Cygnus Loop including new spectra of the filament studied by RBF_G (though with a different slit orientation). They found the width of the broad component of the $H\alpha$ line to be significantly narrower than the value given by RBF_G (130 km s^{-1} compared to 167 km s^{-1} , FWHM). This implied shock velocities of 165 km s^{-1} and 130 km s^{-1} for the cases of rapid and Coulomb equilibration. To reconcile these values

with the far ultraviolet lines which required higher shock velocities, both HRB and L92 suggested that the shock may have decelerated rapidly in the last 200 years or so.

The studies discussed above have established the shock properties in a broad sense. They have shown that the brightest Balmer filaments are due to shocks with velocities between 140 km s^{-1} and 200 km s^{-1} running into gas with a density between about 1 cm^{-3} and 10 cm^{-3} . However, refining the limits on the shock velocity and pre-shock density is crucial for interpreting ultraviolet spectra since the strengths of several diagnostic lines change dramatically in this velocity range (Cox & Raymond 1985). Furthermore, the contradiction in the measured $\text{H}\alpha$ widths measured by RBFG and HRB has not been resolved, and the recent deceleration history of the shock has not been established.

We take a fresh look at this same Balmer filament using the *Hubble Space Telescope* (HST). These observations have the advantage of spatial resolution over the earlier studies. It has been known from theory (e.g. RBFG) that the Balmer emission comes from a very narrow region behind the shock, corresponding to at most a tenth of an arcsecond at the $\sim 440 \text{ pc}$ distance of the Cygnus Loop (Blair et al. 1999). Therefore the earlier observations represent some kind of average over the detailed filament structure. The results from these observations can be re-examined with a knowledge of the subarcsecond structure of the filament. More importantly, the spatial information itself contains diagnostics for the shock properties. For instance, the emissivity of any given line as a function of distance from the shock front depends on the shock velocity and preshock density.

Our study consists of a WFPC2 $\text{H}\alpha$ image and far ultraviolet STIS spectra of the filament. The WFPC2 $\text{H}\alpha$ image shows the structure of the filament in exquisite detail (Blair et al. 1999). The shock wave is an edge-on sheet, gently undulating along the line of sight, with the shock front less than $0''.1$ wide when viewed at exact tangency. In this paper we present the first part of our spectroscopic study using STIS - a far ultraviolet long slit spectrum with the slit placed *perpendicular* to the shock front. This orientation minimizes the effects of curvature of the filaments in the plane of the sky and allows us a relatively clean look at the spatial structure of the shock. The second part (which will be the subject of a future paper) consists of spectra taken with the slit oriented *parallel* to the shock front, and stepped through a grid of positions spanning the width of the filament.

2. Observations

The observations were obtained on April 29, 1999 as part of HST GO program 7289 (PI Blair). The $52'' \times 0''.5$ slit was used along with the G140L grating. The wavelength

coverage is 1118 Å - 1716 Å, and since the source is diffuse and fills the width of the slit, the spectral resolution is ~ 12 Å. Though the slit itself is longer, the effective aperture length in the spatial direction is restricted to 25" by the dimensions of the FUV-MAMA detector. In Figure 1 the effective aperture is shown overlaid on a WFPC2 H α image of the filament. The slit was placed via blind offset after first acquiring a nearby star with an optical peak-up acquisition. Three exposures with a total integration time of 8202 seconds were taken at this position. The brightest part of the filament lying in the slit is at R.A. 20:56:05.80 and DEC. +31:56:13.9 (J2000). In the figure the shock is propagating upwards (i.e. approximately NE); the region below the filament is the interior of the SNR, and the region above is the surrounding interstellar medium (ISM).

In this paper, we are using standard data products generated on February 1, 2000 with the “on the fly” pipeline calibration available from STScI. In this mode, the best available calibration reference files are used. The reduced 2-D spectra for each of the three exposures were co-added. The Ly- α and O I airglow lines at 1216 Å and 1304 Å respectively were subtracted from the 2-D spectrum using line profiles taken along the dispersion axis at a “background” ISM location. Figure 2 shows the resulting 2-D spectrum with annotations indicating the main spectral and spatial features.

The slit passes through three distinct shock tangencies (Figure 1). We will designate the brightest emission near the center as the “bright shock” and the sharp, narrow filaments above and below it as the “north shock” and “south shock” respectively. The spatial positions of these shocks are marked in Figure 2. We note that these shocks are in front of and behind the bright shock only in projection, and physically they are part of the same “sheet” at the edge of the SNR. Furthermore, the bright shock itself has some substructure and may include multiple shock crossings along the line of sight. N V λ 1240, O V λ 1371, C IV λ 1549, He II λ 1640, and the 2-photon continuum from the bright shock are well detected. The N V, C IV and He II lines from the fainter south shock are also detected. Isolating the emission from the north shock is more difficult since the emission from these stronger lines fills the space between the bright and north shocks.

3. Results

In Figure 3, we present the background subtracted spectra of the bright shock and the south shock. We obtained the 1-D spectra by averaging over several rows in the spatial direction, in each case corresponding to $\sim 1''.2$. The background spectrum subtracted from each of these shock spectra was obtained by extracting a $5''.6$ spatial region ahead of the shock, smoothing the result by 3 pixels to lower the noise, and scaling appropriately. The

spectra shown in the plots have been rebinned over 4 pixels (about 0.6 \AA), and the flux at wavelengths covering the Ly- α and O I 1304 \AA airglow lines have been set to zero. The flux units in the plot are $\text{ergs s}^{-1} \text{ cm}^{-2} \text{ arcsec}^{-2} \text{ \AA}^{-1}$. The bright shock spectrum has been offset (arbitrarily) by 0.15 flux units. The N V, C IV and He II lines are seen in both the spectra. The 2-photon continuum is visible in the bright shock spectrum, but is much weaker in the south shock. Additionally, weaker emission from O V, the O IV]-Si IV lines around 1400 \AA and N IV] 1486 \AA is detected in the bright shock spectrum. Although the signal to noise is low, these detections are a remarkable advance in spatial sampling compared with earlier ultraviolet observations (RBF, HRB, L92).

In Table 1 we present the reddening corrected fluxes of some emission lines, relative to N V $\lambda 1240 = 100$, measured in our STIS spectra of the bright and south shocks and in previous studies of the same filament (RBF, L92). Line fluxes in our spectrum were corrected for reddening following L92, who used $E_{B-V} = 0.08$ and the mean galactic extinction curve of Seaton 1979. We find from their Table 1 that the observed, uncorrected fluxes of N V, O V, C IV and He II have to be multiplied by *2.03*, *1.89*, *1.82* and *1.80*, respectively. However, no account has been taken of possible resonance line scattering of N V and C IV photons.

In Table 1 we see that the C IV and He II lines are significantly stronger, relative to N V, in our spectra than in the earlier data. (Due to the low signal, the O V flux we measure is very uncertain and is consistent with L92). The IUE spectra presented by RBF used a $10''$ by $20''$ aperture and the HUT spectrum presented by L92 used a $9''.4$ by $116''$ aperture, whereas the region covered in each of our measurements is approximately $0''.5$ by $1''.2$, immediately behind the Balmer shock front. This is strong evidence that the line ratios depend upon the spatial scale being observed. In particular, the comparison shows that N V emission must come from a more extended region than the C IV and the He II. Similar variations in UV line ratios were seen by HRB in IUE spectra taken at 7 positions along another Balmer filament in the NE Cygnus Loop (their Filament 2). For example, their Table 6 shows that the C IV to N V ratio varied between 0.58 and 1.43. HRB discuss one particular spectrum where N V is stronger than expected and explain the enhanced emission as coming from cooling coronal gas, where the gas was ionized at an earlier time by a shock with a higher velocity.

The distribution of the He II, C IV and N V emitting gas is important for understanding the recent evolution of the shock (and thereby the SNR and surrounding ISM). However, we will postpone further discussion of this subject to Paper II, where we will present several long slit STIS spectra covering a larger spatial region. Now we turn to the spatial structure of the emission just behind the shock fronts.

In Figure 4 we present the observed flux in several lines as a function of position along the slit. The top panel shows the region around the bright shock and the bottom panel shows the region around the south shock. The fluxes (except for $H\alpha$) have been obtained from the STIS spectrum by integrating over the lines along each row; in the case of 2-photon emission, the integration was between 1420 Å and 1460 Å. The $H\alpha$ flux is from the WFPC2 image, taking a cross-cut along the slit, and averaging across its width. The counts in the image were converted to flux units using the prescription given in Holtzman et al. 1995. The peak of the 2-photon emission is chosen as the $x = 0$ position, and x increases towards the interior of the SNR (i.e. shocks move right to left in these plots). The $H\alpha$ emission profile is aligned so that its peak coincides with the 2-photon emission peak. In the plots, the profiles obtained from the STIS spectrum have been binned by 4 pixels ($0''.1$) for the bright shock (top panel) and by 10 pixels ($0''.25$) for the south shock (bottom panel).

The separation between the N V emission zone and the shock front is clearly resolved in the spatial profiles of the bright shock (Figure 4, top panel). This is expected in non-radiative shocks. After entering the shock front the gas takes time to reach successively higher ionization states; and so at a given instant, the ionization state of the gas increases with distance behind the shock front. Therefore, $H\alpha$ and 2-photon emission arise immediately behind the shock front, followed by He II, C IV and then N V emission. The *HST* spectrum has enabled us to partially resolve this stratified structure in a non-radiative SNR shock for the first time. The separation between the C IV and N V emission can also be seen in the noisier south shock profiles (Figure 4, bottom panel). We can quantify the separation between the C IV and N V zones by measuring the locations of the peaks for the bright shock. For the noisier south shock, the offset between the leading edges of the C IV and N V zones is a measure of their separation. We obtain a separation of $0''.30 \pm 0''.10$ for the bright shock and $0''.30 \pm 0''.25$ for the south shock, and use these values in the discussion below. At our assumed distance of the Cygnus Loop (440 pc), $0''.3$ corresponds to about 2×10^{15} cm.

4. Analysis and Discussion

The shock structure, including the intensities and spatial profiles of the ultraviolet lines, depends mainly on the shock velocity and the pre-shock density. In the case of a non-radiative shock, such as the one being considered here, the ionization is not necessarily complete in the post shock flow, and the resulting spectrum is also a function of the swept up column density. Furthermore, the line strengths from any ionization state of an element

heavier than helium scales linearly with the abundance. We can conveniently interpret our data and determine (or constrain) the Balmer filament properties by comparing the observed spectrum with model predictions. We use an updated version of the Raymond shock code (described by Raymond 1979 and Cox & Raymond 1985) to calculate the shock models. The code considers a constant velocity shock running into a uniform medium and calculates the resulting structure, in particular the line emissivities as a function of swept up column (or equivalently of distance behind the shock front). The most important updates for the present investigation are the ability to follow electron and ion temperatures separately and the use of ionization rates based on Coulomb-Born calculations (e. g. Younger 1981).

In order to systematically examine the dependence of the shock spectrum on the shock velocity and pre-shock density, we have run a grid of models varying the shock velocity between 160 km s^{-1} and 200 km s^{-1} in steps of 10 km s^{-1} and with three values of the pre-shock density: 1 cm^{-3} , 2 cm^{-3} and 4 cm^{-3} . We assume abundances representative of the diffuse ISM, taken from Cowie & Songaila 1986. The He, C, N, O, Ne, Mg, Si, S, Ar, Ca, Fe and Ni abundances are 10.99, 8.40, 7.90, 8.70, 8.09, 7.10, 6.50, 7.51, 6.45, 4.61, 5.80 and 4.26 on a scale where the logarithm of the H abundance is 12.00. We are assuming that no elements are liberated from grains due to the shock until after the ultraviolet line formation. This is a valid assumption since the emission region we are considering is formed within about 200 years after the passage of the shock front whereas studies have shown that the time scale for grain destruction due to such shocks is a few thousand years (Jones et al. 1994, Vancura et al. 1994).

In addition to these basic quantities, the shock models require other input parameters. Following RBF, the neutral fraction of the pre-shock gas was taken to be 30% in all cases. (The $\text{H}\alpha$ and 2-photon intensities depend on the density of neutrals entering the shock front. However $\text{Ly}\beta$ photons can also be converted to $\text{H}\alpha$ plus 2-photon continuum and contribute significantly to their intensities. Therefore using the observed $\text{H}\alpha$ and 2-photon intensities to determine the neutral fraction requires detailed analysis of the $\text{Ly}\beta$ radiative transfer, which is beyond the scope of this paper). The extent of equilibration between electrons and ions in the shock front is also unknown (see e. g. Draine & McKee 1993), but Ghavamian 1999 has used Balmer line profiles to show that T_e is at least 80% as large as T_i in a slightly faster shock in the northern Cygnus Loop. In any case, we find that assuming rapid equilibration in the shock front or slower Coulomb equilibration in the post-shock gas has a minor effect on the ultraviolet line strengths and a negligible effect on the spatial profiles. (A similar conclusion was reached by Hartigan 1999). Therefore, in all the models we present, rapid equilibration ($T_e = T_i$ everywhere in the post-shock gas) has been assumed. The value of the pre-shock magnetic field is important in determining the properties of the gas and the grain dynamics in the cooling zone of the post-shock

flow where both the gas and the field are highly compressed. However, the structure and emission properties of the ionization zone that we consider here are independent of the pre-shock field. In all the models, we use a value of $0.1 \mu\text{G}$ for the pre-shock magnetic field. (We find that models using pre-shock fields of $1 \mu\text{G}$ give the same results). The pre-shock gas temperature in all models is $10,000 \text{ K}$ (e. g. HRB).

4.1. An Illustrative Shock Model

Before moving on to the main analysis, we present an example of the emission line structure predicted by a shock model. The example uses a shock velocity of 180 km s^{-1} and a pre-shock density of 2 cm^{-3} which are the “best fit” values found by L92, who compared shock models with their HUT data.

The top panel in Figure 5 shows the emissivities of He II $\lambda 1640$, C IV $\lambda 1549$ and N V $\lambda 1240$, normalized to their respective maxima, plotted as a function of distance behind the shock front. The stratification of the post-shock gas is evident, with emission from the lowest ionization species occurring first. The N V emission zone is well separated from the He II and C IV zones and extends over a larger spatial region.

In the bottom panel of Figure 5 the cumulative intensity (in $\text{ergs s}^{-1} \text{ cm}^{-2}$) of the lines is plotted. The cumulative intensity of a line at a given distance is the intensity in the line produced up to that point in the post-shock flow and coming out of the front of the shock. We see that the He II and C IV intensities level off about $1.5 \times 10^{15} \text{ cm}$ and $3.5 \times 10^{15} \text{ cm}$ behind the shock front while the N V intensity continues to rise. (This is evident from the emissivity plot where the N V zone extends beyond 10^{16} cm). Therefore, for a given shock velocity and pre-shock density, the emission line spectrum depends upon the spatial extent of the post-shock region, which in turn depends on the amount of material swept up by the shock. In these plots we have shown emission out to 10^{16} cm , here corresponding to a swept up column of about $2.1 \times 10^{17} \text{ cm}^{-2}$.

4.2. Spatial Structure

We have calculated the separation between the C IV and N V emission peaks for the grid of models, and we plot the results in Figure 6. The shock velocity is plotted along the x-axis, and different symbols are used to represent models with different pre-shock densities. The separation between the zones decreases with increasing shock velocity, and for a given shock velocity the separation scales linearly with pre-shock density.

The physical separation corresponding to the observed angular separation of $0''.3$ depends on the distance of the Cygnus Loop. We recently found the distance to the Cygnus Loop to be 440_{-100}^{+130} pc, combining the proper motion of the Balmer filament (using our WFPC2 image and a 1953 POSS-I image) with the range of shock velocities found for the filament (Blair et al. 1999). In Figure 6, the dotted line is at 1.97×10^{15} cm, which corresponds to $0''.3$ at 440 pc. The dashed lines are at 1.02×10^{15} cm and 3.41×10^{15} cm, which correspond to $0''.2$ at 340 pc and $0''.4$ at 570 pc. They represent the limits of the observed separation taking into account the distance uncertainty as well as the $\pm 0''.1$ uncertainty in the measurement for the bright shock (§3 and Figure 4).

One of the factors influencing the observed separation is the geometry of the shock front along the line of sight. Curvature will typically have the effect of making the observed separation between the zones larger than the intrinsic separation. In order to make a simple quantitative estimate of this effect, we have assumed that the shock front can be approximated by the arc of a circle. We then integrate the model predicted emissivities along lines of sight that are chords to the circle. Using a radius of curvature of 5×10^{17} cm (estimated from the H α image, Figure 1), we find the following. For the 180 km s^{-1} shock with pre-shock density of 2 cm^{-3} , the separation is increased to 5.9×10^{15} cm and for the 200 km s^{-1} shock with pre-shock density of 4 cm^{-3} , the separation is increased to 2.3×10^{15} cm. Therefore, shocks at the lower end of the velocity range and with lower densities are ruled out by the observed separation. However, shocks with higher velocities and higher densities cannot be ruled out on the basis of these data.

4.3. Line Strengths

As we have seen (§4.1, Figure 5) the shock spectrum for a given shock velocity and pre-shock density depends on the amount of swept up material, or equivalently on the width of the post-shock region. In order to compare the grid of models with the observed spectrum, we need to specify this parameter. The spectrum in Figure 3 and the line strengths (from our observations) in Table 1 are based on a $1''.2$ region behind the shock front. This corresponds to about 8×10^{15} cm at 440 pc. We therefore fix the width of the post-shock region in the shock models to be this value. Truncated in this way, the swept up column density depends most strongly on the pre-shock density (and is largely independent of the shock velocity). In our grid of models, these column densities are approximately $4 \times 10^{16} \text{ cm}^{-2}$, $8 \times 10^{16} \text{ cm}^{-2}$, and $17 \times 10^{16} \text{ cm}^{-2}$ for pre-shock densities of 1, 2 and 4 cm^{-3} , respectively.

In Figure 7 we plot the N V intensities predicted by the models. As in Figure 6,

the shock velocity is plotted along the x-axis and different symbols are used for different pre-shock densities. The N V intensity increases with pre-shock density (as is expected), since a greater column of gas is swept up. The N V intensity decreases with increasing shock velocity. This happens because temperatures in the post-shock gas go as the square of the shock velocity (Raymond 1991) and in faster shocks, elements are ionized to higher stages (e. g. N VI for nitrogen) more rapidly. This results in fewer collisional excitations that lead to the production of line photons.

The intensities shown in Figure 7 apply to the case when the shock is viewed face-on. The Cygnus Loop filament however represents the other extreme - a shock viewed more or less tangentially. Therefore, in order to compare with the predictions, the observed value has to be corrected for viewing angle and geometry. The correction factor is the ratio of the actual shock area observed to the projected shock area. This observed intensity has to be divided by this aspect ratio to obtain the predicted “face-on” intensity. From a ground based H α image of the filaments in this region, HRB estimated an aspect ratio of 10 for the *diffuse* (i. e. least tangential) emission. From the WFPC2 H α image (presented by Blair et al. 1999), we find that the aspect ratio could easily be as high as 50 for bright filaments. The reddening corrected, N V intensity of the bright shock is $3.6 \times 10^{-15} \text{ erg s}^{-1} \text{ cm}^{-2} \text{ arcsec}^{-2}$ (Table 1 and §3). For an aspect ratio of 50, this corresponds to a model predicted value of $7.2 \times 10^{-17} \text{ erg s}^{-1} \text{ cm}^{-2} \text{ arcsec}^{-2}$, which is shown as a dotted line in Figure 7.

The discussion above shows that the range of shock properties we have considered predicts the N V intensity more or less correctly. However, our rather crude estimate of the aspect ratio from the morphology of the filaments in the plane of the sky cannot be used to place very strong constraints on the shock properties. For instance, if the aspect ratio were higher or lower by a factor of 2 for the observed region, the measured N V intensity would be compatible with many of the models. It would be very difficult, though, to reconcile the observed value with the $n_0 = 1 \text{ cm}^{-3}$ models – the predicted intensity is far too low. Recalling that the C IV – N V separation also rules out the low density, low velocity, models (Figure 6), we conclude that the pre-shock gas ahead of the non-radiative filament has a density of at least 2 cm^{-3} .

In Figure 8 we plot the C IV to N V line ratio for the grid of models (truncated at a width of $8 \times 10^{15} \text{ cm}$). The C IV to N V ratio is higher for lower values of pre-shock density because the swept up column density is lower and the N V zone is less complete (see Figure 5). The dependence of this ratio on shock velocity is more subtle - since it is affected both by the swept up column and the rate of ionization to higher ionization states. The observed C IV to N V ratio, corrected for reddening is 1.01 for the bright shock 0.84 for the south shock. These values are consistent with the shock models having pre-shock

densities of 2 and 4 cm⁻³. However, as we discuss below, the intrinsic ratio of C IV to N V can be affected by resonance line scattering.

The edge-on viewing angle implies that we are looking through a relatively large column of emitting gas. The optical depth of the N V and C IV lines, which are ground state transitions, can get high enough to significantly attenuate the line intensities. To estimate the effect of resonance line scattering, we have used the emission profiles from our illustrative model (§4.1), assumed a single shock front with a fixed radius of curvature (i. e. that it is an arc of a circle), and calculated optical depths along tangential lines of sight. We find that the C IV optical depth ($\tau_{\text{C IV}}$) is invariably higher than the N V optical depth ($\tau_{\text{N V}}$). We also find that the ratio $\tau_{\text{C IV}}/\tau_{\text{N V}}$ increases with increasing optical depth (of either line). Specifically, for a radius of curvature 2×10^{17} cm, $\tau_{\text{C IV}} = 1.6$ and $\tau_{\text{N V}} = 1.2$ and for a radius of curvature 1×10^{18} cm, $\tau_{\text{C IV}} = 3.7$ and $\tau_{\text{N V}} = 2.6$. We note that in calculating the optical depths we have assumed that the kinetic temperature of the heavy ions is equal to the proton temperature. If the ionic temperatures are higher (as is the case for the remnant SN1006, Raymond, Blair & Long 1995), the lines will be broader and optical depths correspondingly lower.

The attenuation of the line intensity for a given optical depth, assuming single scattering, is $(1 - e^{-\tau})/\tau$. For the cases mentioned above, the intrinsic ratio of C IV to N V would be higher than the observed ratio by factors of 1.1 and 1.5 for the smaller and larger radii of curvature, respectively. The intrinsic N V intensity in these two cases would be 1.7 and 2.8 times the observed (dereddened) intensity. In the context of our models, a C IV to N V ratio of 1.5 would imply that the pre-shock density is somewhat lower than 2 cm⁻³ (Figure 8). For this “high optical depth” case, the N V intensity assuming an aspect ratio of 50, would be about 2×10^{-16} erg s⁻¹ cm⁻² arcsec⁻². (That is, the dashed line in Figure 7 would have to be placed much higher). Then, to make the observation consistent with a low pre-shock density, the aspect ratio would have to be over 200 (rather than 50), which is extreme. Our models therefore favor a scenario where the N V and C IV optical depths are modest, and the lines are not highly attenuated. We note, however, that our treatment is very simplistic. To make accurate models for the observed emission, a detailed treatment of the line scattering using a realistic geometry is needed.

The observed value of the He II to N V line ratio, corrected for reddening is 1.36 for the bright shock. Models predict much lower values - between about 0.1 and 0.4. The model does not take into account the production of the 1640Å line by He II Ly β 256Å photons and so a lower predicted flux is expected (e. g. RBF). Hartigan 1999 has calculated the expected He II λ 1640 flux for a range of shock velocities. From Figure 1 of that paper, we find that our model predictions need to be corrected by factors of

between 2 and 5. Additionally, any attenuation of N V due to resonance scattering would increase the observed He II to N V ratio, leading to a better match between models and observation. The models predict O V to N V of about 0.08, which is lower than the observed, reddening corrected value of 0.19 for the bright shock. However in this case, the error in the observation is large enough that this difference may not be an issue. Again, resonance scattering of N V would increase the observed O V to N V ratio.

In conclusion, we point out that there are two kinds of uncertainty associated with comparing model line strengths with the observations. First, the observed intensity has to be converted to an intrinsic shock intensity and the conversion depends on the shock geometry along the line of sight as well as the effects of resonance line scattering. Second, the intensities are functions of the elemental abundances, and of the cutoff column density both of which are input parameters for the models. For our chosen ISM abundances, and reasonable geometries, we find that the observations favor shock velocities $\sim 170 \text{ km s}^{-1}$ and preshock densities between 2 and 4 cm^{-3} .

5. Concluding Remarks

We have presented a far-ultraviolet spectrum of a non-radiative filament on the north-east limb of the Cygnus Loop, obtained with STIS. The slit length (and hence the spatial axis of the spectrum) was chosen to be perpendicular to the filament, and therefore perpendicular to the shock front. The brightest lines detected in the 1118Å - 1716Å passband were N V $\lambda 1240$, C IV $\lambda 1549$ and He II $\lambda 1640$. The effective spatial resolution of the spectrum, $\sim 0''.1$, is an improvement over previous studies of the same filament and is important because it allows us to separate the emission from individual shock fronts and also to measure the separation of the C IV and N V emission zones in the post-shock flow. For a given shock front, the observed C IV to N V and He II to N V line ratios in our STIS spectrum are significantly higher than in spectra taken by IUE and HUT covering larger areas (several square arcseconds). This difference is most probably due to a spatially extended component of N V emission, such as cooling gas ionized at an earlier time as suggested by HRB. We have compared our spectrum with a grid of shock models and find that the observed separation of $0''.3$ between the C IV and N V zones excludes pre-shock densities $\lesssim 2 \text{ cm}^{-3}$ for shock velocities $\leq 180 \text{ km s}^{-1}$. (These models predict much larger separations between the zones). Furthermore, models with pre-shock densities $\lesssim 2 \text{ cm}^{-3}$ predict much weaker N V and C IV than observed (assuming ISM abundances and a reasonable path length of emitting gas along the line of sight).

As the premier example of a remnant whose optical and ultraviolet emission is

dominated by shocks due to the interaction of the SN blast wave with the surrounding ISM, the Cygnus Loop plays an important role in our understanding of “middle-aged” SNRs. The spatial scale of the emission from the shocks responsible for the brightest Balmer filaments is a few times 10^{15} cm. This means (as we have shown) that at the 440 pc distance of the Cygnus Loop, the detailed structure of the filaments can be resolved by HST. Observations of the filaments at this high resolution are critical for a correct understanding of the shock conditions, since lower resolution observations average over larger regions which in general contain a complex substructure. (We again point out the difference between our and earlier spectra of the same filament, Table 1). On the theoretical side, we need a realistic 3-dimensional model for the shock geometry and the ability to compute the effects of resonance line scattering. This would refine our interpretation of the observed spectra and place more stringent limits on the shock conditions responsible for the Cygnus Loop Balmer filaments.

This work has been supported by STScI grant GO-07289.01-96A to the Johns Hopkins University.

REFERENCES

- Blair, W. P., Sankrit, R., Raymond, J. C., & Long, K. S. 1999, *AJ*, 118, 942
- Chevalier, R. A., Kirshner, R. P. & Raymond, J. C. 1980, *ApJ*, 235, 186
- Cowie, L. L., & Songaila, A. 1986, *ARA&A*, 24, 499
- Cox, D. P., & Raymond, J. C. 1985, *ApJ*, 298, 651
- Draine, B. T., & McKee, C. F. 1993, *ARA&A*, 31, 373
- Fesen, R. A., & Itoh, H. 1985, *ApJ*, 293, 43
- Ghavamian, P. 1999, Ph. D. Thesis, Rice University
- Hartigan, P. 1999, *ApJ*, 526, 274
- Hester, J. J., Raymond, J. C., & Blair, W. P. 1994, *ApJ*, 420, 721 (HRB)
- Holtzman, J. A., Burrows, C. J., Casertano, S., Hester, J. J., Trauger, J. T., Watson, A. M., & Worthey, G. 1995, *PASP*, 107, 1065
- Jones, A. P., Tielens, A. G. G. M., Hollenbach, D. J., & McKee, C. F. 1994, *ApJ*, 433, 797
- Long, K. S., Blair, W. P., Vancura, O., Bowers, C. W., Davidsen, A. F., & Raymond, J. C. 1992, *ApJ*, 400, 214 (L92)
- Raymond, J. C. 1979, *ApJS*, 39, 1
- Raymond, J. C. 1991, *PASP*, 103, 781
- Raymond, J. C., Blair, W. P., Fesen, R. A., & Gull, T. R. 1983, *ApJ*, 275, 636 (RBFSG)
- Raymond, J. C., Blair, W. P., & Long, K. S. 1995, *ApJ*, 454, L31
- Seaton, M. J. 1979, *MNRAS*, 187, 73P
- Vancura, O., Raymond, J. C., Dwek, E., Blair, W. P., Long, K. S., & Foster, S. 1994, *ApJ*, 431, 188
- Younger, S. M. 1981, *J. Quant. Spec. Radiat. Transf.*, 26, 329

Fig. 1.— The slit position for the STIS spectrum is shown, overlaid on a WFPC2-H α image of the non-radiative filament (from Blair et al. 1999). The box represents the slit, which is 0".5 wide and has an effective length (determined by the FUV MAMA detector) of 25". The image uses a logarithmic stretch and is scaled to bring out the shock structures along the slit.

Fig. 2.— The pipeline calibrated 2D spectrum of the non-radiative shock obtained with STIS. The 0".5 slit and G140L grating were used. Several spectral and spatial features are labeled on the figure. The “bright shock” corresponds to the brightest H α emission seen in the slit in Figure 1. (Note that due to remapping done by the STIS pipeline, the bright shock is off-center in the 2D spectrum while it is near the slit center in the image. Strong airglow lines (Ly α and O I λ 1304) have been subtracted to first order.

Fig. 3.— Background subtracted spectra of the bright shock and the south shock. The spectra were generated by averaging over several rows in the spatial direction, corresponding to $\sim 1".2$. The background was obtained by averaging over a $5".6$ region outside the SNR shock and smoothing over 3 pixels. The spectra shown in the figure have been rebinned by 4 pixels ($\sim 0.6 \text{ \AA}$) and the flux at wavelengths covering the Ly α and O I 1304 \AA airglow lines have been set to zero. F_λ has units of $\text{ergs s}^{-1} \text{ cm}^{-2} \text{ arcsec}^{-2} \text{ \AA}^{-1}$.

Fig. 4.— The observed flux in various lines as a function of position along the slit for the bright shock (top panel) and the south shock (bottom panel). The peak 2-photon and H α emission have been aligned and chosen to be at $x = 0$, with x increasing towards the interior of the SNR (i.e. shocks move right to left in these plots). The flux units are $10^{-15} \text{ ergs s}^{-1} \text{ cm}^{-2} \text{ arcsec}^{-2}$ and normalized as shown. Note the offset of the N V profile in both bright and south shocks.

Fig. 5.— Predicted emission from a shock model with velocity 180 km s^{-1} and pre-shock density of 2 cm^{-3} . The normalized emissivity (*top panel*) and cumulative intensity (*bottom panel*) of the three brightest ultraviolet lines detected in the STIS spectrum are shown as a function of distance behind the shock. The intensity plotted in the bottom panel refers to the amount of emission coming out of the front of the shock and has units of $\text{ergs s}^{-1} \text{ cm}^{-2}$. The angular scale bar of 0".3 assumes a distance of 440 pc to the Cygnus Loop. Note how the N V is produced over a much broader region than the other lines.

Fig. 6.— The plot shows the separation between the peak positions of the C IV and N V emission predicted by a set of shock models. The separation is shown as a function of shock velocity for different values of the pre-shock density (shown by different symbols). The dotted line corresponds to the observed separation of 0".3 (Figure 4) at 440 pc. The dashed lines indicate the limits of the separation taking into account the uncertainty in the measured

separation and the uncertainty in the distance.

Fig. 7.— The plot shows the N V intensities predicted by the models. The models were truncated at a distance of $\sim 8 \times 10^{15}$ cm behind the shock front. As in Figure 6, the shock velocity is plotted along the x-axis and different symbols are used for different pre-shock densities. The dotted line shows the observed, de-reddened bright shock intensity divided by 50, to correct for the aspect ratio.

Fig. 8.— The plot shows the C IV to N V line ratio for the models, truncated (as in Figure 7) at $\sim 8 \times 10^{15}$ cm behind the shock front.

Table 1. Observed line strengths

Ion	λ	Bright	South	RBF	L92
N V	1240	100	100	100	100
O V	1371	19	14
C IV	1549	101	84	71	63
He II	1640	136	154	48	42

Note. — These are observed values, corrected for reddening. The corrected N V intensities for the bright and south shocks are 3.61 and 1.08×10^{-15} erg s⁻¹ cm⁻² arcsec⁻².

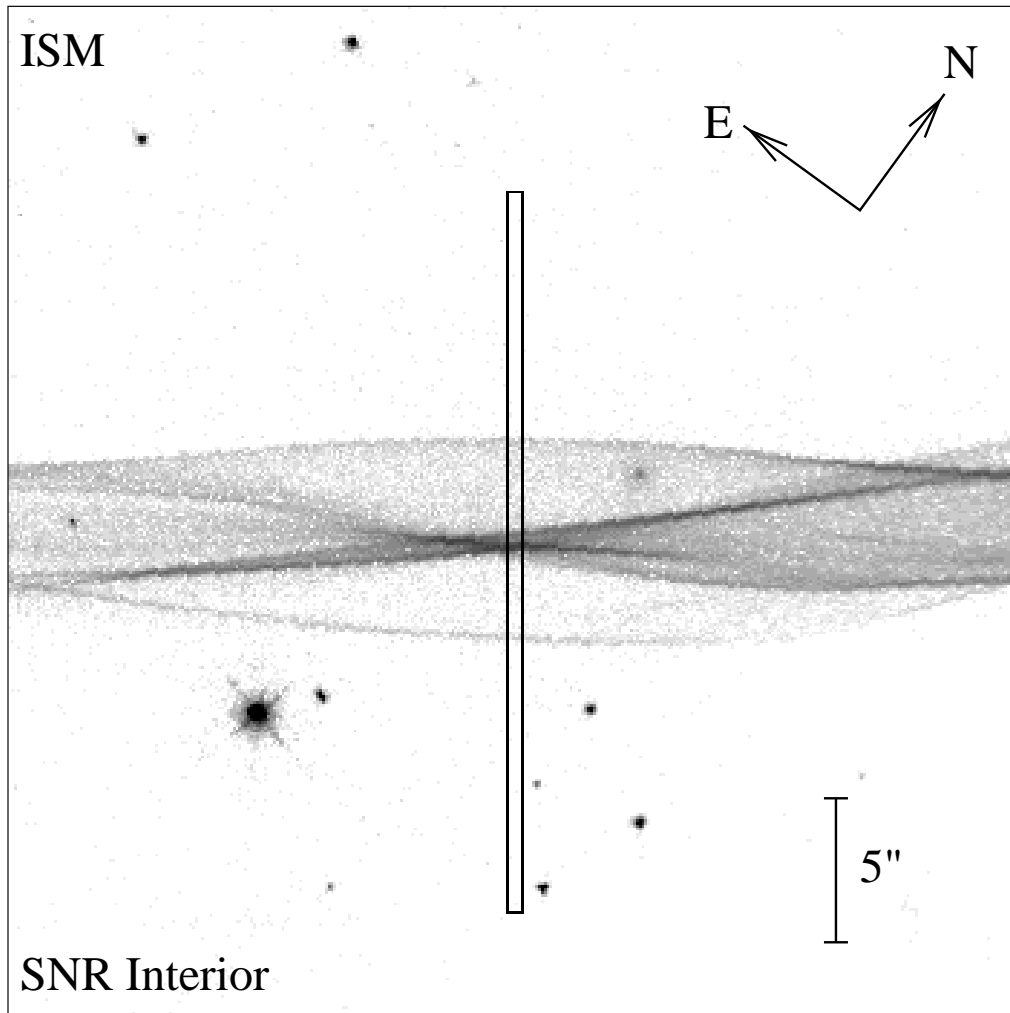


Fig. 1

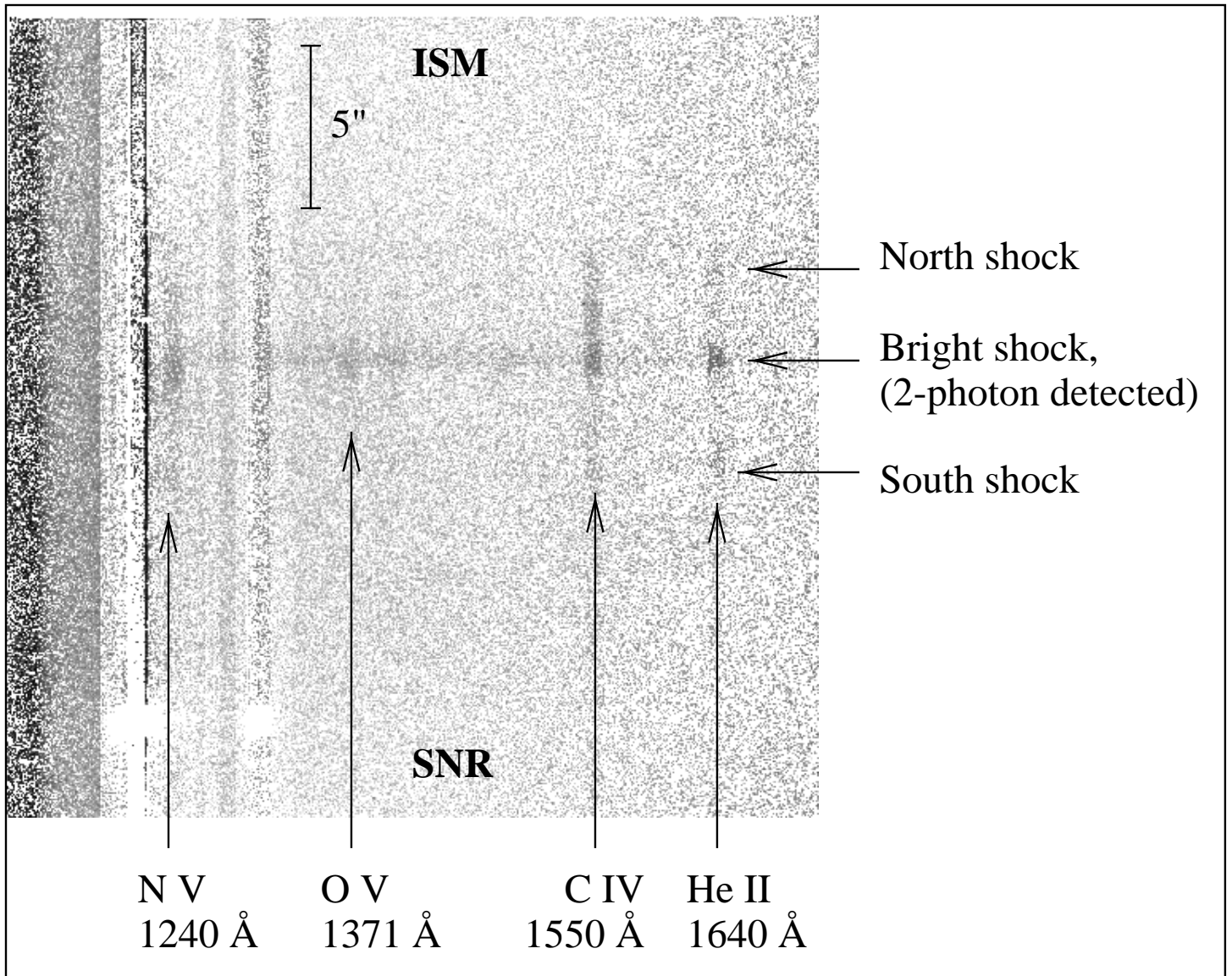


Fig. 2

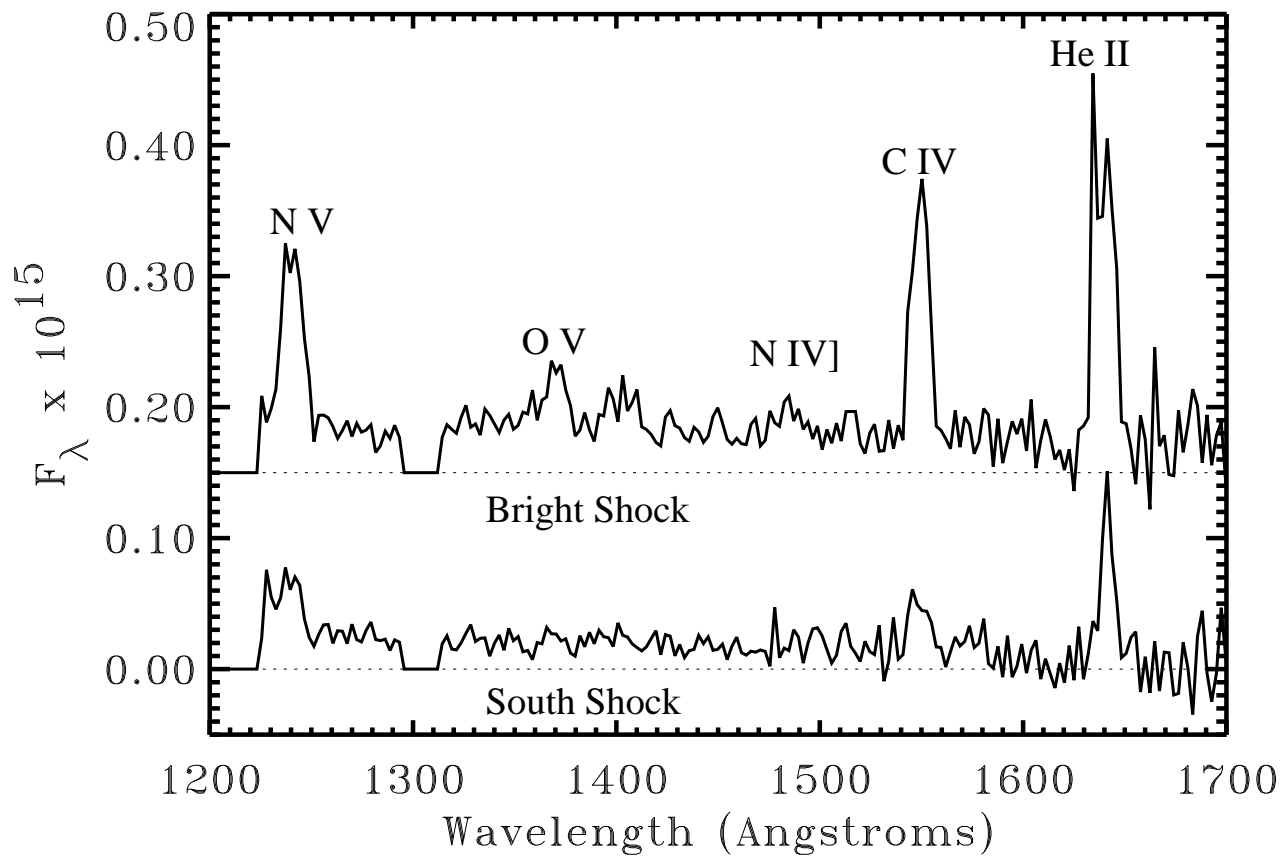


Fig. 3

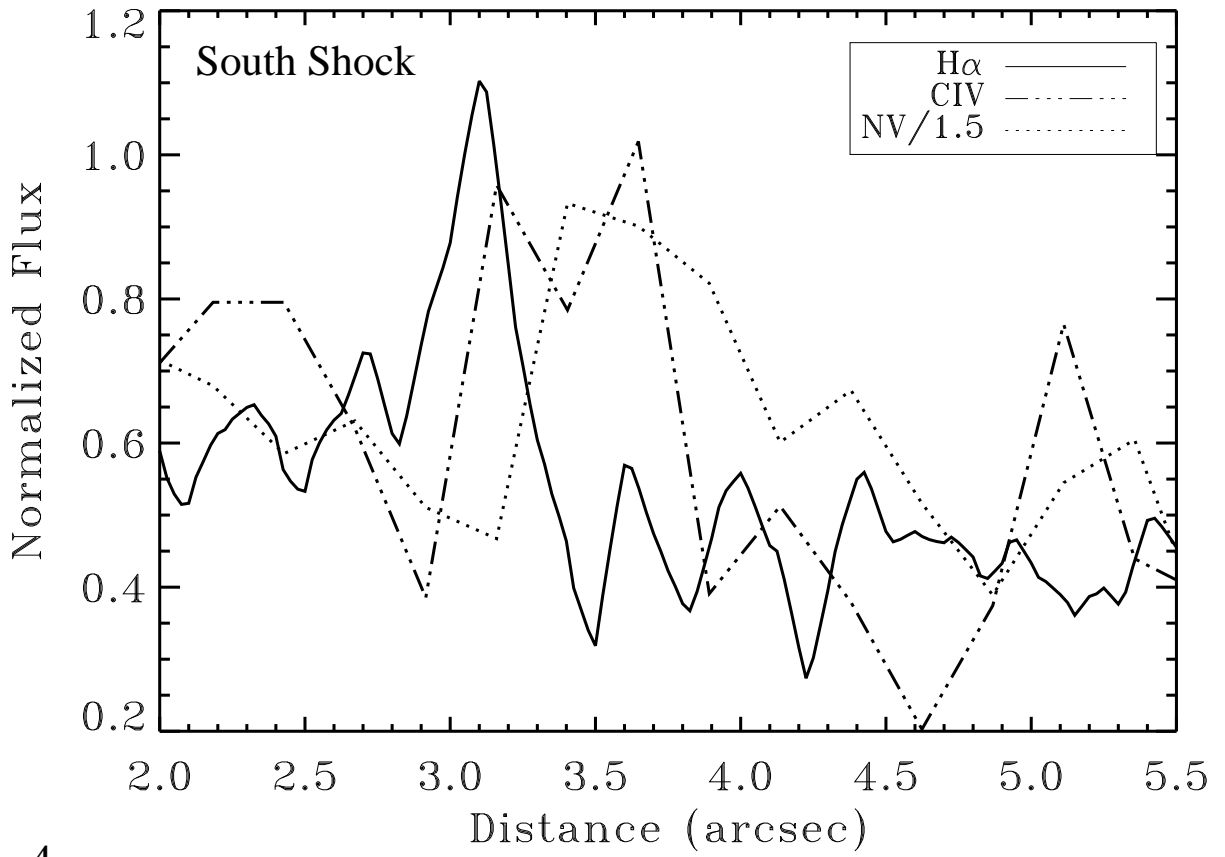
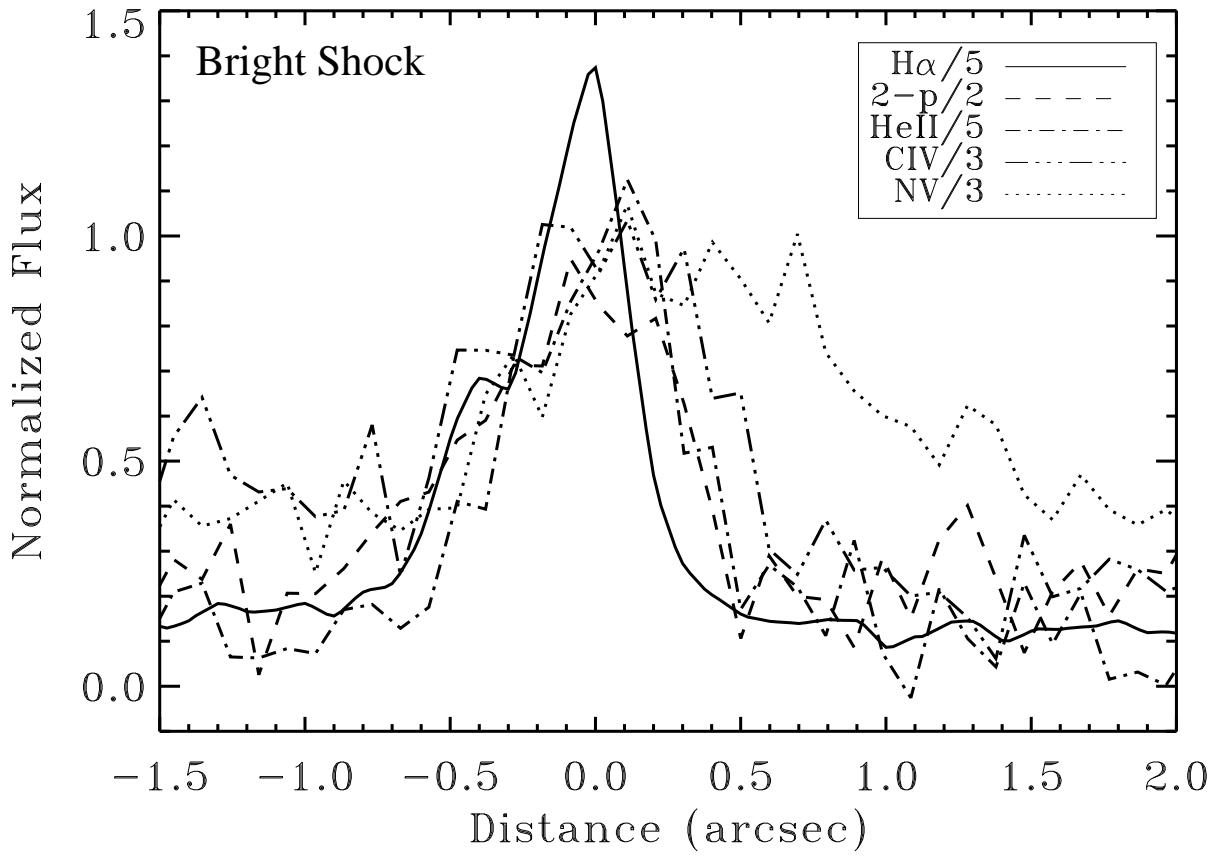


Fig. 4

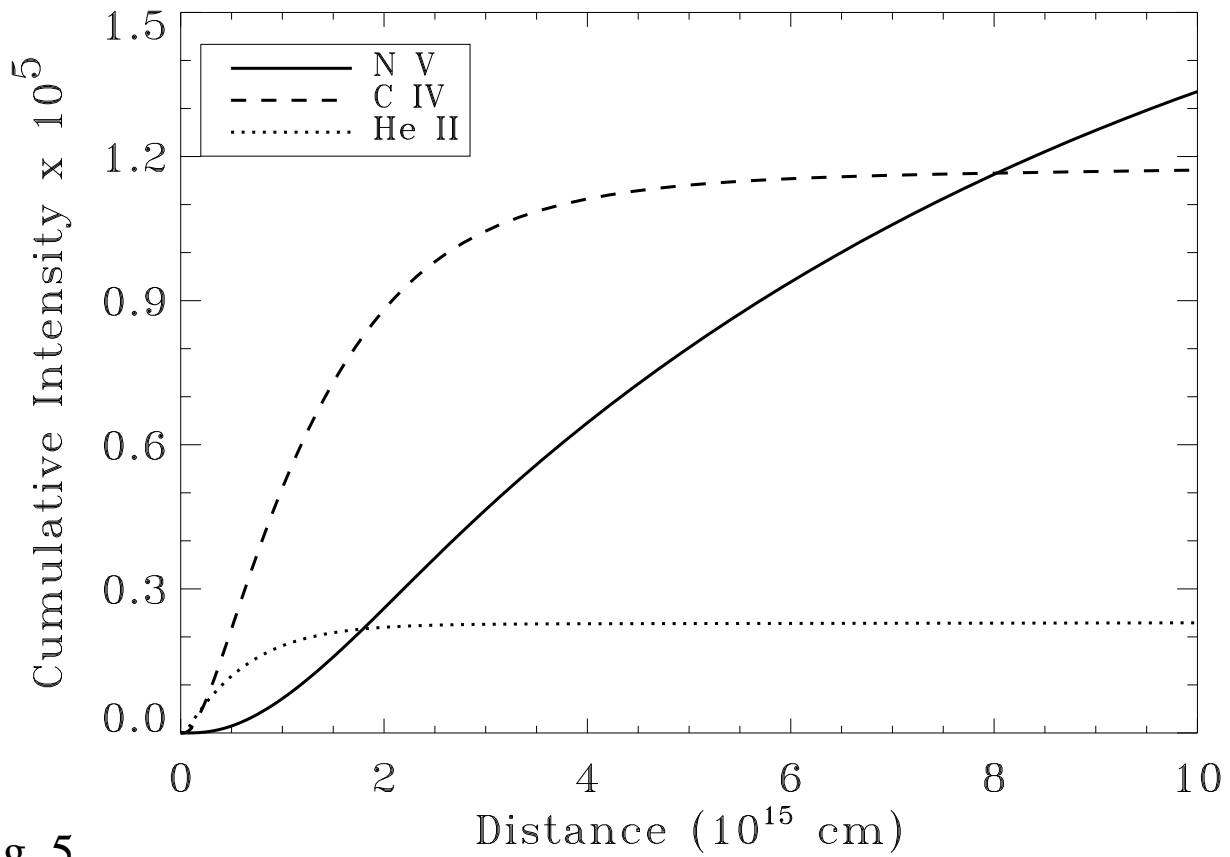
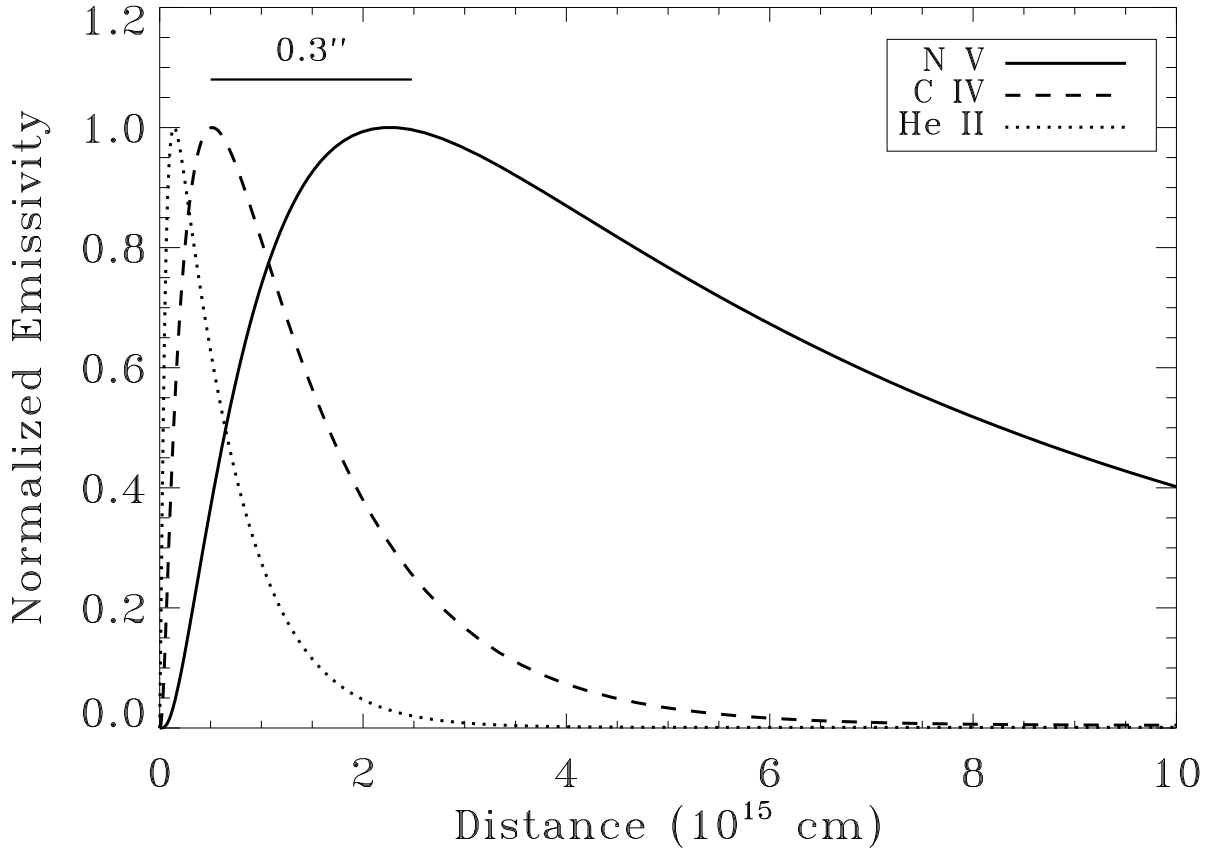


Fig. 5

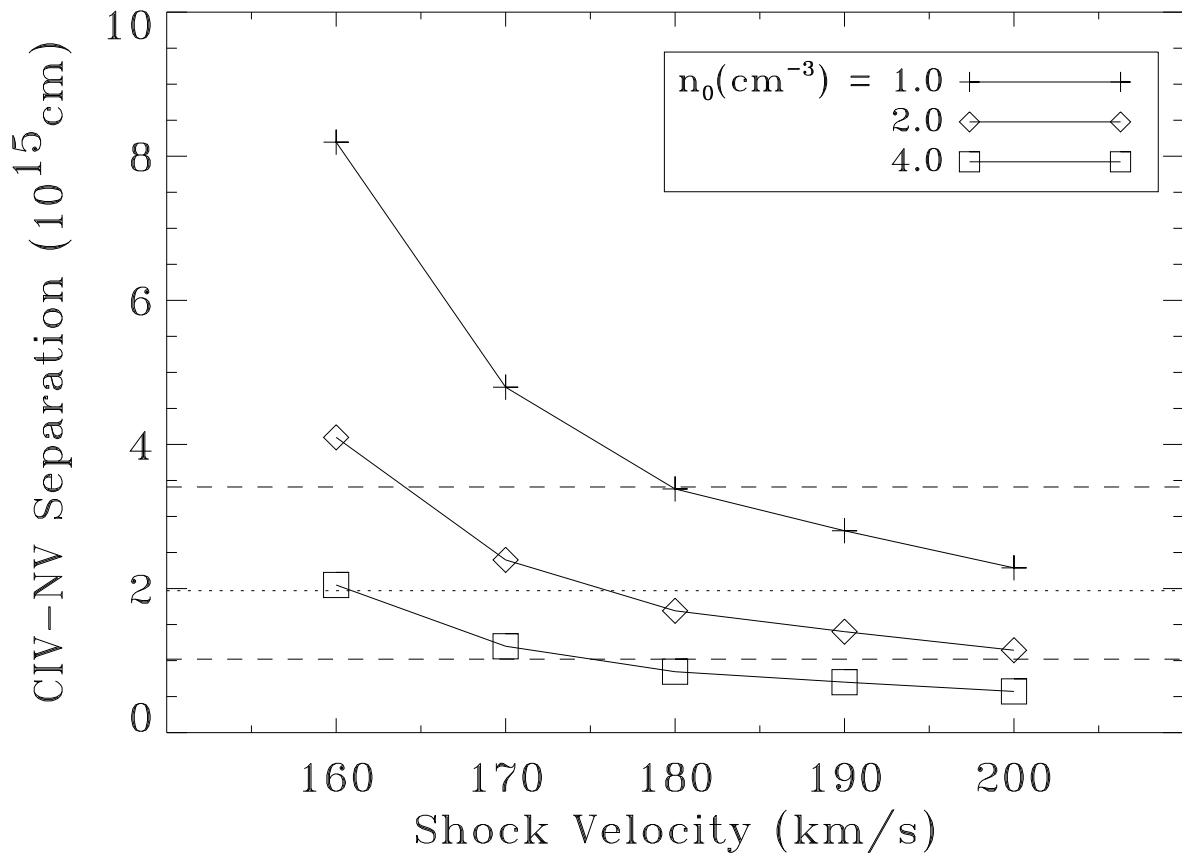


Fig. 6

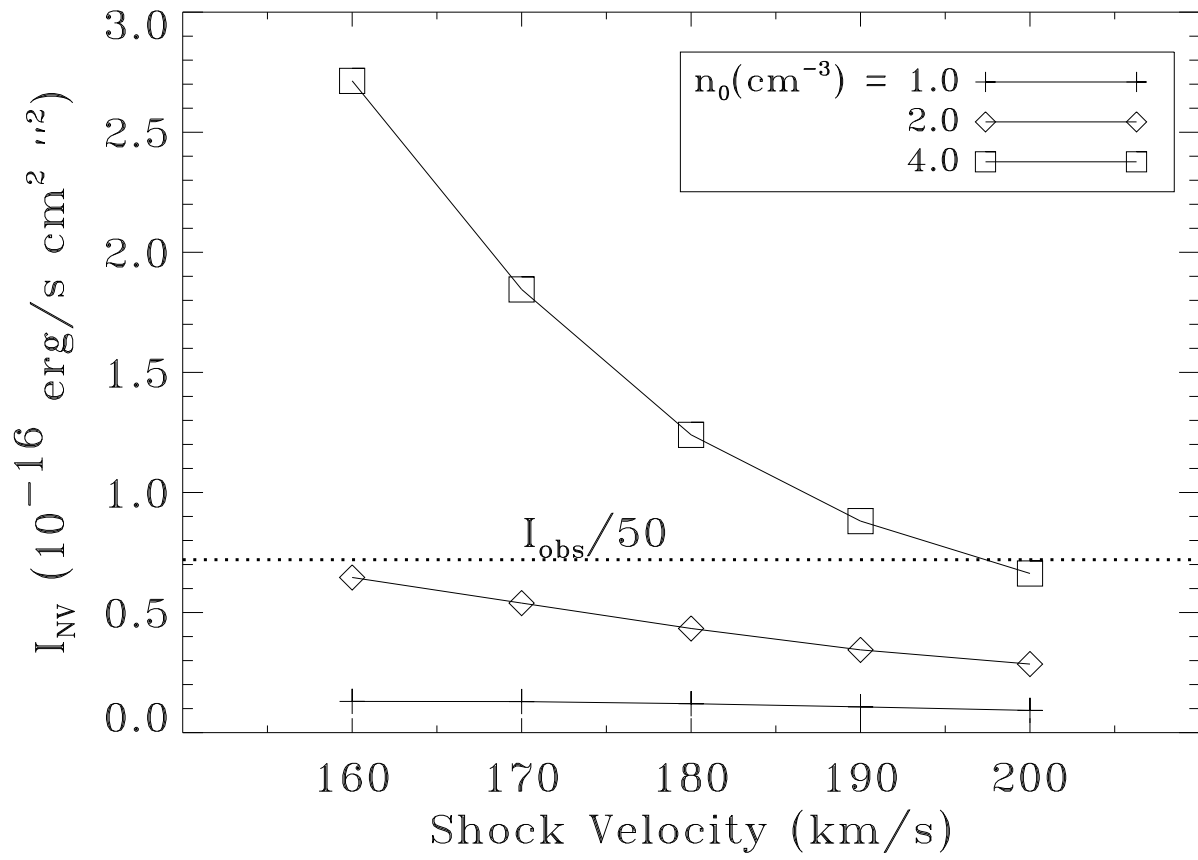


Fig. 7

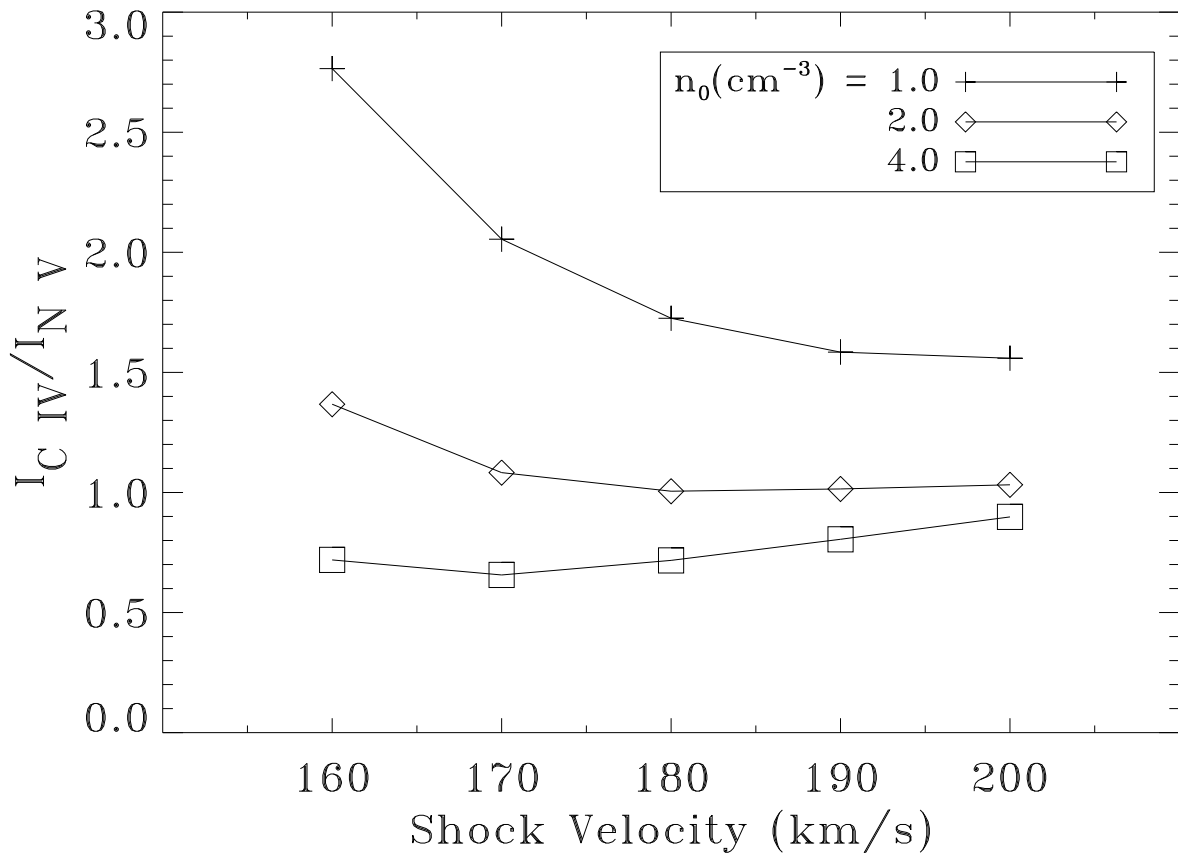


Fig. 8